Rydberg atomic antenna in strongly driven multielectron atoms

Stefanos Carlström,[1,2,*] Jan Marcus Dahlström,[2] Misha Yu Ivanov,[1,3,4] and Serguei Patchkovskii[1]

[1]*Max-Born-Institut, Max-Born-Straße 2A, 12489 Berlin, Germany*

[2]*Department of Physics, Lund University, Box 118, SE-221 00 Lund, Sweden*

[3]*Department of Physics, Imperial College London, South Kensington Campus, London SW72AZ, United Kingdom*

[4]*Institut für Physik, Humboldt-Universität zu Berlin, Newtonstraße 15, 12487 Berlin, Germany*

(Received 3 May 2022; accepted 22 September 2022; published 24 October 2022)

We study the role of intermediate excitations of Rydberg states as an example of Kuchiev's "atomic antenna" in above-threshold ionization of xenon, in particular their effect on the coherence between the spin-orbit-split states of the ion. We focus on the case of a laser frequency close to resonant with the spin-orbit splitting, where a symmetry (parity) argument would preclude any coherence being directly generated by strong-field ionization. Using *ab initio* simulations of coupled multielectron spin-orbit dynamics in strong laser fields, we show how field-driven rescattering of the trapped Rydberg electrons introduces efficient coupling between the spin-orbit-split channels, leading to substantial coherences, exceeding 10% for some photon energies.

DOI: 10.1103/PhysRevA.106.043114

I. INTRODUCTION

Spin-orbit effects are usually neglected in the interaction with strong infrared (IR) fields. A few exceptions include the development of consistent treatment within the R-matrix method [1], recent experiments [2,3] on imaging the spin-orbit breathing of a hole created by strong-field ionization, and the generation of spin-polarized photoelectrons [4] following the proposal of [5,6]. In all these cases [2–6], the dipole approximation holds, ensuring that no transitions between the spin-orbit-split states were induced by the incident IR field.

In this article we show that, even in the dipole approximation, strong IR fields trigger transitions between the spin-orbit-split states of the ion via a mechanism resembling the "atomic antenna" of Kuchiev [7]. In our case, an active electron driven by a strong IR field is trapped in a long-lived Rydberg orbit. Oscillating in the IR field, it transfers the energy to the core via nondipole electron-electron interaction. This atomic antenna breaks the dynamic symmetry with respect to the polarization of the linearly polarized driving laser field [8]. It thereby induces coherence between the spin-orbit-split states of the ion, reduces the entanglement between the ion and the photoelectron, and manifests itself in the photoelectron spectra.

This article is arranged as follows: in Sec. II, we introduce the degree of coherence between ionic states and discuss why parity-conservation arguments require the coherence to vanish when the photon energy matches the spin-orbit splitting; in Sec. III, we present the main computational results that contradict these expectations, as well as our explanation. Finally, Sec. IV concludes the article.

II. THEORY

We consider a xenon atom, initially in the ground state, interacting with an IR pulse with carrier photon energy $\hbar\omega$ close to the spin-orbit splitting of the cation, $\Delta E_{\rm so} \approx 1.3\,\text{eV}$, $\eta \stackrel{\text{def}}{=} \hbar\omega/\Delta E_{\rm so} \sim 1$ (atomic units $\hbar = e = a_0 = m_{\rm e} = 1$ are used in the following). Our calculations include all relevant electronic excitations (i.e., single excitations or ionizations from $5s_{1/2}$, $5p_{1/2}$, or $5p_{3/2}$ are allowed) and account for spin-orbit coupling effects. We solve the time-dependent Schrödinger equation in the dipole approximation and the length gauge for a configuration-interaction singles (CIS) ansatz that allows single excitation or ionization from a Hartree–Fock reference [9–14]. The spin-orbit interaction is treated using an energy-consistent relativistic effective-core potential [15] (see [16] for an alternative option based on the four-component Dirac equation). Ion-resolved above-threshold ionization (ATI) photoelectron spectra are computed [14] using the surface flux techniques with Volkov asymptotics [17–22]. From these spectra, we compute the reduced density matrix $\{\rho_{IJ}\}$, obtained by tracing over the photoelectron degrees of freedom. We then form the normalized *degree of coherence*:

$$\tilde{\rho}_{IJ} \stackrel{\text{def}}{=} \frac{\rho_{IJ}}{\sqrt{\rho_{II}\rho_{JJ}}}, \tag{1}$$

where ρ_{IJ} is the coherence between I and J and ρ_{II} and ρ_{JJ} are the populations in ion states I and J, respectively. Further details are given in Appendix A.

*stefanos@mbi-berlin.de; stefanos.carlstrom@matfys.lth.se

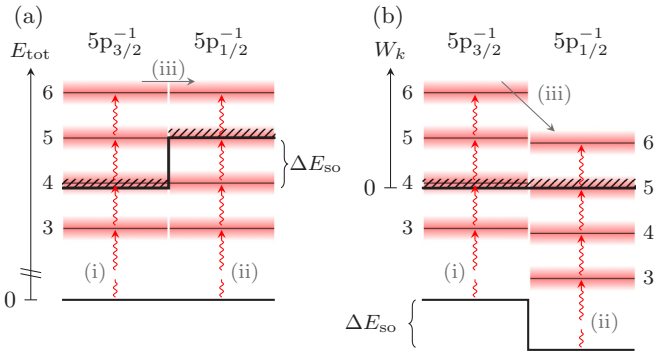

FIG. 1. Sketch of the energy diagram for ATI from xenon for $\eta \stackrel{\rm def}{=} \hbar\omega/\Delta E_{\rm so} = 0.9$; the numbers indicate the number of photons necessary to reach a certain final energy. The three most important pathways are (i) direct ionization into the $5p_{3/2}^{-1}$ channel including elastic rescattering, (ii) direct ionization or elastic rescattering in the $5p_{1/2}^{-1}$ channel, and (iii) indirect contributions due to inelastic rescattering from $5p_{3/2}^{-1}$ to $5p_{1/2}^{-1}$ (this dominates over rescattering in the other direction). (a) Total energy (photoelectron + ion), relative to the field-free neutral atom. In this picture, the energy conservation in inelastic scattering is easily seen. (b) Energies of the photoelectrons in each channel. Nonzero photoelectron overlap is necessary for coherence between the ion cores to exist. For $\eta \sim 1$, photoelectrons with similar kinetic energies are due to the absorption of a different number of photons.

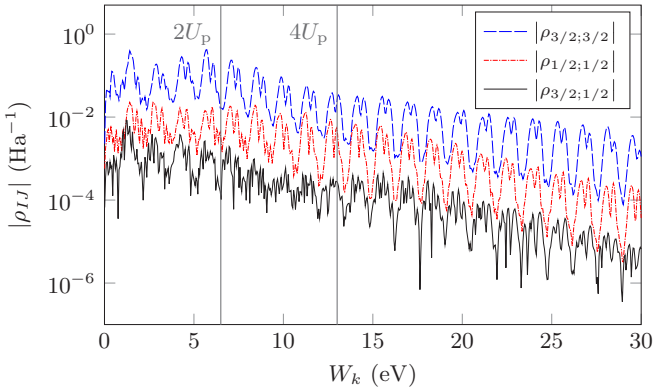

FIG. 2. Calculated ATI spectrum of xenon using $4.4 \times 10^{13}\,\mathrm{W/cm^2}$ with $\eta \approx 0.96$ and a pulse duration of 30 fs. The dashed blue line is the photoelectron spectrum $\rho_{3/2;3/2}$ correlated with the $5p_{3/2}^{-1}$ ionization channel; the dot-dashed red line is the corresponding spectrum $\rho_{1/2;1/2}$ for the $5p_{1/2}^{-1}$ channel, and the black solid line is the energy-resolved coherence $\rho_{3/2;1/2}$ between the two channels. Above approximately $4U_{\rm p}$, the spectrum in $5p_{1/2}^{-1}$ and the coherence exhibit structures which are very similar to the spectrum in $5p_{3/2}^{-1}$; we infer that the $5p_{1/2}^{-1}$ channel is populated almost exclusively through rescattering in this energy region [see (iii) in Fig. 1].

Let us first consider coherence between the spin-orbit-split states of the ion generated by ionization [3,6,23–26]. The final state of the system "ion + photoelectron" is

$$\begin{aligned}|\Psi\rangle &= |I\rangle|\chi_I\rangle + |J\rangle|\chi_J\rangle \\ &= (|I\rangle + |J\rangle w)|\chi_I\rangle + |J\rangle(|\chi_J\rangle - w|\chi_I\rangle),\end{aligned} \tag{2}$$

where we choose $w \stackrel{\rm def}{=} \langle\chi_I|\chi_J\rangle$ as a measure of the factorizability of the wave function and antisymmetrization with respect to the coordinates of the photoelectron is implied. Coherent spin-orbit dynamics in the ion requires nonzero overlap between the continuum electron wave packets correlated to the ionic states $|I\rangle$ and $|J\rangle$, respectively: $w \neq 0$. Perfect overlap $|w| = 1$ corresponds to a 100% degree of coherence since (2) factorizes into

$$|\Psi\rangle = (|I\rangle + e^{i\phi}|J\rangle)|\chi\rangle$$

for some phase ϕ. Perfect electron–ion entanglement corresponds to $w = 0$.

By a symmetry argument, zero coherence and perfect entanglement are expected for $\eta = 1$: nonzero coherence and hence $w \neq 0$ require that the two photoelectron wave packets overlap in energy. After absorption of q photons of energy ω, the photoelectron energy is

$$\begin{aligned}W_k &= q\omega - I_{{\rm p},I} - U_{\rm p} - \frac{\delta\alpha_I}{4}F^2 \\ &= q\omega - I_{{\rm p},I} - U_{\rm p}(1 + \omega^2\delta\alpha_I),\end{aligned} \tag{3}$$

where ω is the driving laser frequency, $I_{{\rm p},I}$ is the ionization potential in ionization channel I, $U_{\rm p} = F^2/4\omega^2$ is the *ponderomotive potential* of the electric field with peak amplitude F, and $\delta\alpha_I$ is the difference between the polarizabilities of the ground state of the neutral and the state of the ion. For $\eta \sim 1$, the photoelectron peaks correlated with the $5p_{3/2}^{-1}$ and $5p_{1/2}^{-1}$ ion cores coincide in energy when one extra photon is absorbed in the $5p_{1/2}^{-1}$ channel (see Fig. 1). Thus, the photoelectron associated with $5p_{3/2}^{-1}$ would have opposite parity compared to $5p_{1/2}^{-1}$, while the $5p_{3/2}^{-1}$ and $5p_{1/2}^{-1}$ ion cores have the same parity. The overall parity would thus be opposite between the channels, implying $w = 0$ by symmetry, precluding any coherence. If very short, broadband pulses are used, a nonzero coherence can, nonetheless, result due to the energetic overlap of two successive ATI peaks belonging to the two thresholds. This is the mechanism behind the coherence observed by Goulielmakis *et al.* [3], who use pulses of 3.8-fs duration. This coherence diminishes when longer pulses are used and is expected to disappear entirely for the much longer pulses ($\geqslant 15$ fs) used in the present work.

III. RESULTS

We begin by considering ionization by a 30-fs pulse, tuned just below the spin-orbit splitting ($\eta = 0.96$). As can be seen from the simulation results in Fig. 2, there is nonzero coherence between $5p_{3/2}^{-1}$ and $5p_{1/2}^{-1}$, where the ATI peaks in the respective channels overlap energetically. Figure 3 shows the calculated degree of coherence (1) between the $5p_{3/2}^{-1}$ and $5p_{1/2}^{-1}$ ion cores as a function of η. Contrary to the symmetry-based expectation, we see substantial coherence, even exceeding 10% for some η. We trace its origin to frustrated tunneling [27–29]—trapping of the electron into Rydberg states after optical tunneling from the ground state. Once the neutral atom is "parked" in the intermediate, excited state for an extended amount of time, there is an opportunity to undergo multiple successive (Stokes-)Raman transitions that each increase the system energy by a small amount while

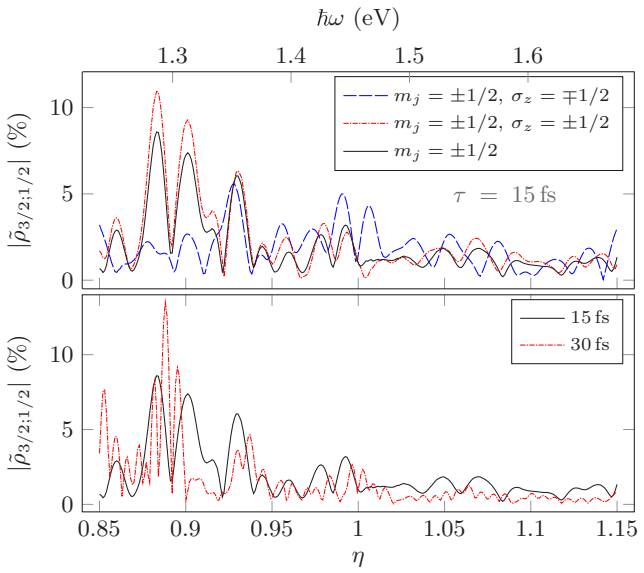

FIG. 3. Ionic coherence in xenon. Top: the degree of coherence [Eq. (1)] between ionization channels $5p_{3/2}^{-1}$ and $5p_{1/2}^{-1}$ as a function of the ratio η between the photon energy and the spin-orbit splitting, resolved on the m_j quantum number of the ion and the spin σ_z of the photoelectron. Due to the cylindrical symmetry of the ionization process, there is a mirror symmetry in the combinations of m_j and σ_z. Additionally, tracing out σ_z leads to the final degrees of coherence for $m_j = \pm 1/2$, which coincide. Bottom: the degree of coherence for two different pulse durations (solid black line: $\tau = 15$ fs, dot-dashed red line: $\tau = 30$ fs).

conserving the parity. After multiple such Raman transitions have occurred, the energy may increase enough to bridge the energy gap to the next ATI order. Upon subsequent ionization and rescattering into the other ion channel, the overlap of photoelectrons of the same parity and energy explains the observed coherence.

In the frequency domain, frustrated tunneling followed by ionization corresponds to the so-called *Freeman resonances* [30] imprinted on top of the photoelectron peaks. The apparent "parity violation" is a manifestation of the dynamic symmetry being broken due to the simultaneous presence of the Freeman resonances and the spin-orbit interaction. The Freeman resonances introduce memory in the time evolution, breaking time-reversal symmetry, or, equivalently, spatial-inversion symmetry between the responses of the system to two successive half cycles. Simultaneously, the spin-orbit coupling leads to the mixing of the ionic spin-orbit channels. Together, these two effects demote the photoelectron parity from a selection rule to a *propensity rule* [8]. We stress that parity conservation of the *whole* wave function may *not* be violated, whereas there is no such guarantee for the constituent parts. That parity with respect to the ℓ quantum number of the photoelectron is only a propensity rule has also been observed in an analogous example in single-photon spectroscopy of xenon [31,32], where it has also been linked to the interaction with the core electrons.

The atomic antenna by Kuchiev [7] lends a complementary perspective: the intermediate excited Rydberg states of the neutral are, in some aspects, very similar to free electrons. A resonance structure is built up in the (Stark-shifted) quasicontinuum of the Rydberg states, which, similar to an antenna, can be used to channel energy into the system and thereby drive transitions in the ion core. It is, of course, necessary that the antenna is "sensitive" to the radiation $\hbar\omega$ impinging on it, such that it may efficiently couple the energy into the system; this is the case if a pair of Rydberg states is separated by $\hbar\omega$. Furthermore, one or both of the states involved in the transition must bridge the ion manifold, i.e., have components in both the $5p_{3/2}^{-1}$ and $5p_{1/2}^{-1}$ manifolds. A few of the likely candidates for the antenna transitions are listed in Table I. This is the frequency-domain perspective of the inelastic rescattering. To confirm the antenna picture, we have investigated transitions for which $\eta \in [0.85, 1.15]$ and their strengths. The details are given in Appendix B, along with alternative explanations that we have considered, such as depletion, envelope effects, and single-state coherence. To further investigate the role of the Rydberg states excited via the Freeman resonances, we perform a Fourier transform of the degree of coherence along the η axis. This analysis reveals quantum beat periods of the excited wave packet, which constitute a fingerprint of the atomic antenna. By inverting the quantum beat periods, we instead get the energy separation between neighboring antenna transitions, which is shown in Fig. 4. As is evident from Fig. 4, the very complex coherence patterns in Fig. 3 are, in fact, due to a small number of individual antenna transitions. These

TABLE I. Some dipole-allowed transitions in xenon [33] which are likely candidates for the antenna transition, given their energies and compositions.

ΔE_{ki} (eV)	i Configuration	Term	k Configuration	Term
1.353	$5p^5(^2P^o_{3/2})6s$	$^2[3/2]^o_1$	$5p^5(^2P^o_{3/2})6p$	$^2[3/2]_1$
1.332	$5p^5(^2P^o_{1/2})6s$	$^2[1/2]^o_1$	$5p^5(^2P^o_{3/2})7p$	$^2[1/2]_1$
1.265	$5p^5(^2P^o_{3/2})6s$	$^2[3/2]^o_2$	$5p^5(^2P^o_{3/2})6p$	$^2[1/2]_1$
1.249	$5p^5(^2P^o_{3/2})6s$	$^2[3/2]^o_1$	$5p^5(^2P^o_{3/2})6p$	$^2[5/2]_2$

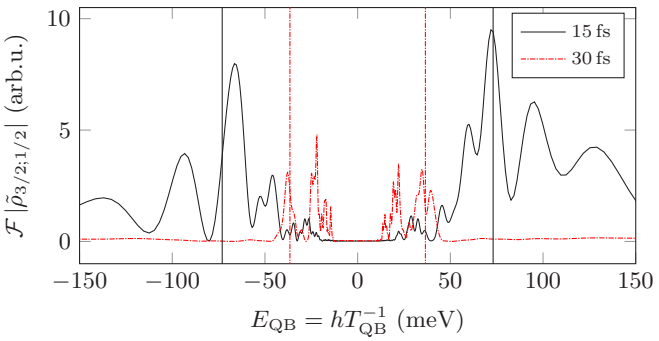

FIG. 4. Fourier transform of the degree of coherence depicted in Fig. 3 for the two different pulse durations (solid black line: $\tau = 15$ fs, dot-dashed red line: $\tau = 30$ fs). Since $\hbar\omega \equiv \eta\Delta E_{\mathrm{so}}$ has the dimension of energy, the conjugate variable has the dimension of time. Here, we instead plot the peaks as a function of the quantum beat *energy* E_{QB}, i.e., the energy separation between neighboring antenna transitions. The vertical lines indicate the spectral width of the driving pulse, $\delta E = \hbar\sqrt{4\ln 2}\,\tau^{-1}$, which is ∼73.1 meV for $\tau = 15$ fs and ∼36.5 meV for $\tau = 30$ fs.

transitions occur for energy separations close to the bandwidth of the driving pulse. This is not an accident: transitions at these energies reach an optimal balance between the available photon fluence (decreasing away from the carrier frequency, making the transition less likely) and the number of photons needed to be emitted or absorbed to close the spin-orbit gap, which decreases for larger energy separations (increasing the transition probability). When the pulse duration increases, the spectral bandwidth decreases. This imposes stricter requirements on which antenna transitions are in resonance with the driving field with photon energy $\hbar\omega$. It is more likely that we will find such transitions among the higher-lying states in the Rydberg quasicontinuum, which are more closely spaced energetically. This explains why, for the longer pulse duration, we observe in Fig. 4 quantum beat components of the wave packet with comparatively smaller E_{QB}, corresponding to the more tightly spaced peaks in Fig. 3.

This circumstance also helps us understand why the longer pulse duration can produce *larger* degrees of coherence when we might have expected the opposite; decreasing spectral bandwidth leads to narrower photoelectron peaks [34], which in turn lead to smaller energetic overlap between the ATI progressions. However, as long we are in resonance with the antenna, a longer pulse is beneficial since we can transfer population into the different pathways while maintaining coherence. This is reminiscent of the previously studied case of weak-photon ionization of xenon [35], where longer pulse durations also led to increased ionic coherence, albeit for a simpler resonance condition.

We emphasize that, although the electron-electron interaction is crucial for the effectiveness of the antenna mechanism, the initial asymmetry is created by the laser field, which imposes the natural quantization axis on the system. The asymmetry is then transferred to the electron spin through the spin-orbit interaction (electron spins do not couple to the laser field in the dipole approximation). Finally, the electron-electron interaction provides very efficient coupling between the Rydberg electron (the antenna) and the ion core. Thus, all three interactions are essential, with each playing a distinct role in the process.

IV. CONCLUSIONS

We have shown that through the intermediate Rydberg-state dynamics, we can introduce coherence between ionization pathways that would otherwise have opposite parity by symmetry. The coherence is sensitive to the frequency and duration of the ionizing laser pulse and allows us to identify the effect of the Rydberg atomic antenna essentially background free.

ACKNOWLEDGMENTS

We would like to acknowledge the help of the late O. Zatsarinny in estimating the viability of this project. The work of S.C. has been supported through scholarship 185-608 from Stiftelsen Olle Engkvist Byggmästare. J.M.D. acknowledges support from the Knut and Alice Wallenberg Foundation (Grants No. 2017.0104 and No. 2019.0154), the Swedish Research Council (Grant No. 2018-03845), and Stiftelsen Olle Engkvist Byggmästare (Grant No. 194-0734). M.Y.I. acknowledges support from Deutsche Forschungsgemeinschaft (Grant No. IV 152/10-1).

APPENDIX A: METHODS

We employ Hartree atomic units and implied summation and integration over indices, orbitals, momenta, and/or spins appearing on only one side of an equation.

1. Grid-based time-dependent configuration-interaction singles

The derivation of the equations of motion (EOMs) and a detailed description of the propagator are given in [14]; the EOMs agree with those of Rohringer *et al.* [12], Greenman *et al.* [13], apart from the fact that spin restriction is *not* imposed in the present work, i.e., we are solving the two-component Schrödinger equation.

The time-dependent CIS EOMs describe the time evolution of the amplitude c_0 for the Hartree–Fock reference state and the particle orbital $|\tilde{k}\rangle$ emanating from the occupied (time-independent) orbital $|k\rangle$. The different particle-hole channels can couple via either the laser interaction or the Coulomb interaction:

$$\begin{aligned} i\partial_t c_0 &= \langle k|\hat{V}_L|\tilde{k}\rangle, \\ i\partial_t|\tilde{k}\rangle &= (-\epsilon_k + \hat{f})|\tilde{k}\rangle + c_0\hat{V}_L|k\rangle - \langle l|\hat{V}_L|k\rangle|\tilde{l}\rangle \\ &\quad - (\hat{J}_{lk} - \hat{K}_{lk})|\tilde{k}\rangle - \lambda_{\tilde{k}i}|i\rangle, \end{aligned} \tag{A1}$$

where ϵ_k is the field-free energy of the occupied orbital $|k\rangle$, $(\hat{f} - \hat{V}_L - \epsilon_k)|k\rangle = 0$; the Fock operator is defined as $\hat{f} \stackrel{\text{def}}{=} \hat{h} + \hat{J}_{ii} - \hat{K}_{ii}$, with the one-body Hamiltonian containing the interaction with the external laser field, $\hat{h} \stackrel{\text{def}}{=} p^2/2 + \hat{V}_C(\boldsymbol{r}) + \hat{V}_L$; $\hat{V}_L \stackrel{\text{def}}{=} \boldsymbol{F}(t)\cdot\boldsymbol{r}$; and the *direct* and *exchange interaction* potentials are given by their action on an orbital,

$$\begin{aligned} \hat{J}_{cd}|e\rangle &\stackrel{\text{def}}{=} \chi_e(\varsigma_1)\int \frac{d\varsigma_2}{|\boldsymbol{r}_1 - \boldsymbol{r}_2|}\chi_c^*(\varsigma_2)\chi_d(\varsigma_2), \\ \hat{K}_{cd}|e\rangle &\stackrel{\text{def}}{=} \chi_d(\varsigma_1)\int \frac{d\varsigma_2}{|\boldsymbol{r}_1 - \boldsymbol{r}_2|}\chi_c^*(\varsigma_2)\chi_e(\varsigma_2) \equiv \hat{J}_{ce}|d\rangle, \end{aligned}$$

where $\varsigma_{1,2}$ refer to both spatial and spin coordinates of the orbitals. As we consider atoms in the present work, the particle orbitals $|\tilde{k}\rangle\,|\tilde{l}\rangle\cdots$ are conveniently expanded in a tensor product basis formed from spinor spherical harmonics (i.e., $n\ell jm_j$; see Sec. 7.2 of [36]) and finite differences for the radial dimension [37,38]. Finally, the Lagrange multiplier $\lambda_{\tilde{k}i}$ ensures that $|\tilde{k}\rangle$ remains orthogonal to the occupied orbital $|i\rangle$ at all times.

Because we are working in the dipole approximation, $\hat{V}_L$ includes only E_1 transitions. As discussed in the main text, $5p_{3/2}^{-1}$ and $5p_{1/2}^{-1}$ have the same parity, which means $\langle 5p_{3/2}^{-1}|\hat{V}_L|5p_{1/2}^{-1}\rangle = 0$. However, even if the dipole-forbidden (E_2 and M_1) transitions between $5p_{3/2}^{-1}$ and $5p_{1/2}^{-1}$ were to be included, they would be so minuscule [39,40] that the resulting coherence would be $\sim 10^{-7}$ to $\sim 10^{-9}$. Instead, in our simulations we find coherence of $\sim 10^{-2}$ for *all* $\eta \sim 1$.

TABLE II. Calculated ionization potentials of the $5\{s, p\}$ electrons of xenon, compared with their experimental values. The corresponding Keldysh parameters, for the range of photon energies used, indicate that ionization is in a regime intermediate between the multiphoton and tunneling limits.

Hole	I_p (eV)	Expt. [33] (eV)	Δ (eV)	Keldysh γ
$5s_{1/2}^{-1}$	27.927	23.397	4.530	1.84–2.25
$5p_{1/2}^{-1}$	13.483	13.436	0.047	1.28–1.73
$5p_{3/2}^{-1}$	12.026	12.130	−0.104	1.21–1.63

2. Atomic structure and pulse parameters

The EOMs (A1) as formulated would yield the same result as a one-component calculation; that is, there would be no effect due to the spin of the electrons. To implement spin-orbit coupling (as well as corrections due to scalar-relativistic effects) and at the same time reduce the number of electrons we need to treat in the calculation, we replace the scalar potential $\hat{V}_C$ by the relativistic effective core potential (RECP) of Peterson *et al.* [15], which models the nucleus and the $1s$–$3d$ electrons according to

$$\hat{V}_{\rm PP}(\boldsymbol{r}) = -\frac{Q}{r} + B_{\ell j}^k \exp\big(-\beta_{\ell j}^k r^2\big)\hat{P}_{\ell j},$$

where $Q = 26$ is the residual charge, $\hat{P}_{\ell j}$ is a projector on the spin-angular symmetry ℓj, and $B_{\ell j}^k$ and $\beta_{\ell j}^k$ are numeric coefficients found by fitting to multiconfigurational Dirac-Fock all-electron calculations of the excited spectrum. For a thorough introduction to RECPs, see, e.g., the review by Dolg and Cao [41].

The radial grid consists of 527 points extending to 90.4 bohrs with the spacing smoothly varying according to [38]

$$r_j = r_{j-1} + \rho_{\rm min} + (1 - e^{-\alpha r_{j-1}})(\rho_{\rm max} - \rho_{\rm min}),$$

with $r_1 = \rho_{\rm min}/2$, $\rho_{\rm min} = 0.1154$ bohr, $\rho_{\rm max} = 0.1768$ bohr, and $\alpha = 0.3$. The spin-angular grid is limited to $\Delta m_j = 0$ since we consider only linearly polarized light. For pulses with a duration of 15 fs we use $\ell_{\rm max} = 40$, and for a 30-fs duration we use $\ell_{\rm max} = 60$.

Finally, since the calculation is performed in a finite computational domain, we use Manolopoulos's [42] transmission-free *complex-absorbing potential* covering the last 12.57 bohrs at the far end of the box, with a design parameter $\delta \approx 0.21$; this choice gives <1% reflection for photoelectrons with kinetic energies above 3.4 eV ($\Longleftrightarrow$ $k_{\rm min} = 0.5$ a.u.).

With these grid parameters, the ionization potentials for the xenon model (only $5s$ and $5p$ orbitals are allowed to ionize) are given in Table II; the calculated spin-orbit splitting is approximately $\Delta E_{\rm so} \approx 1.46$ eV. The deviation from the experimental ionization potential is much larger for $5s_{1/2}^{-1}$; this is to be expected at the CIS level of theory, where the ion is not allowed to relax. This is, however, immaterial for the present work since its ionization fraction is negligible.

The driving-field frequency is scanned across the range $\eta \overset{\rm def}{=} \hbar\omega/\Delta E_{\rm so} \in [0.85, 1.15]$ $\Rightarrow \hbar\omega = 1.24$ to 1.68 eV, and its intensity $I_0 = 4.4 \times 10^{13}\,{\rm W/cm^2}$ $\Rightarrow U_p = 4.12$ to 2.25 eV is chosen such that the ionization remains at the level of a few percent. The pulse duration is 15 or 30 fs, and the pulse shape is a smoothly truncated Gaussian [43], with $t_1 = 25.5$ fs, $t_2 = 38.2$ fs and $t_1 = 51.0$ fs, $t_2 = 76.4$ fs, respectively. The time propagator is second order accurate, and 2000 steps per carrier cycle are taken, which yields a time step τ varying from 1.67 to 1.23 as for the range of values of η quoted above.

3. Photoelectron spectra and ion coherences

Photoelectron spectra are computed using a multichannel extension [14] of the surface flux techniques with Volkov asymptotics [17–22], yielding the familiar close-coupling [44] decomposition of the wave function, resolved on final ion state I, and photoelectron momentum $\boldsymbol{k}$ and spin σ_z (it is assumed that the ion and photoelectron are sufficiently separated, such that antisymmetrization can be safely omitted):

$$|\Psi\rangle = c_{I\boldsymbol{k}\sigma_z}|I\rangle|\boldsymbol{k}\sigma_z\rangle.$$

From this long-range ansatz, we can form the density matrix of the total system

$$\hat{\rho}_{I\boldsymbol{k}'\sigma_z';J\boldsymbol{k}''\sigma_z''} \overset{\rm def}{=} |\Psi\rangle\langle\Psi| = c_{I\boldsymbol{k}'\sigma_z'}|\boldsymbol{k}'\sigma_z'\rangle|I\rangle\langle J|\langle\boldsymbol{k}''\sigma_z''|c^*_{J\boldsymbol{k}''\sigma_z''}$$

and, by subsequently tracing out the photoelectron, the *reduced density matrix*, expressing the coherence between ion states,

$$\rho_{IJ} = \langle\boldsymbol{k}\sigma_z|\langle I|\hat{\rho}|J\rangle|\boldsymbol{k}\sigma_z\rangle = c_{I\boldsymbol{k}\sigma_z}c^*_{J\boldsymbol{k}\sigma_z}$$

(the population for the ion state I is $\rho_I \equiv \rho_{II}$). These quantities are used to compute the degree of coherence as shown in Eq. (1).

APPENDIX B: CONFIRMING THE ATOMIC ANTENNA

Below, we will discuss various aspects of the atomic antenna [7] and avenues we have pursued to confirm that this proposed mechanism is, indeed, responsible for the observed symmetry breaking and nonvanishing coherence.

1. Influence of depletion

Since the degree of coherence is on the order of a few percent, similar to the level of ionization for the intensity chosen, an alternative explanation could be depletion-induced residual coherence. This would be a memory effect, similar to hole burning, deviating from the cycle-to-cycle adiabaticity and breaking the time-translation symmetry [45,46]. To rule out this possibility, we artificially prevented the depletion of the ground state by renormalizing the ground-state amplitude after every time step, which did not appreciably change the final coherence.

2. Dynamical effects due to the envelope

We also investigated whether the dynamical ac Stark shift of the Rydberg states due to the envelope of the laser field had any influence on the coherence. Substituting the Gaussian envelope with a flattop pulse removes most of the dynamical shifts, leaving only a constant ac Stark shift. The degree of coherence was mostly unaffected by this change, increasing by only a few percent.

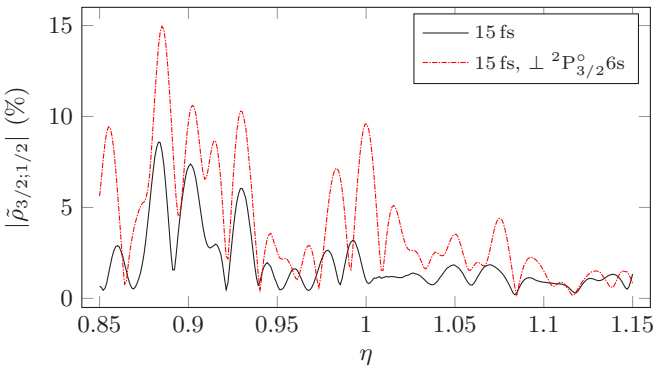

FIG. 5. Effect on the degree of coherence from removing $5p_{3/2}^{-1}$ 6*s* from the calculation [see Eq. (B1)]; the black solid line shows the degree of coherence for a 15-fs pulse (the same as seen in Fig. 3 in the main text), and the red dot-dashed line shows the degree of coherence for the same pulse, but with $5p_{3/2}^{-1}$ 6*s* projected out.

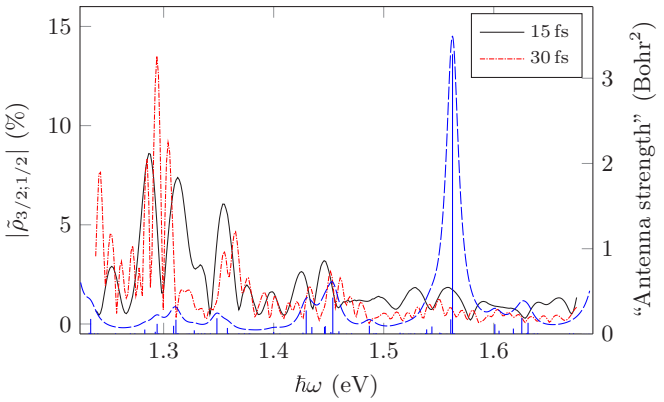

FIG. 6. Antenna transitions: The left ordinate corresponds to the degree of coherence for 15 and 30 fs, shown by the solid black and dot-dashed red lines, respectively. The right ordinate corresponds to the antenna strengths, computed using (B2) and shown as sticks and convoluted with a Lorentzian spectral shape (B3), shown as the dashed blue line.

3. Removing one Rydberg state

We next consider the effects of specific Rydberg states; we begin by confirming that the Rydberg states, populated via frustrated tunneling, are important in the formation of the antenna. To test this hypothesis we repeated the calculation while preventing the $5p_{3/2}^{-1}$ 6*s* state from being intermediately excited *via the laser interaction*. The propagator $\mathcal{U}_L$ for the laser interaction $\hat{V}_L$ is replaced according to

$$\mathcal{U}_L \to \hat{P}\mathcal{U}_L\hat{P} + \hat{Q}, \tag{B1}$$

where $\hat{Q}$ is the projector onto the $5p_{3/2}^{-1}$ 6*s* state and $\hat{P} \equiv \hat{\mathbf{1}} - \hat{Q}$ is the projector onto the orthogonal complement. In this way, the $5p_{3/2}^{-1}$ 6*s* state is still present in the calculation, but it will not be coupled via the laser field; we can do this since in the length gauge, the field-free excited state remains a good approximation of the time-dependent eigenstate. The state chosen has an $\sim$0.979 contribution from the $5p_{3/2}^{-1}$ manifold, an $\sim 1.95 \times 10^{-2}$ contribution from $5p_{1/2}^{-1}$, and an $\sim 1.82 \times 10^{-3}$ contribution from $5s_{1/2}^{-1}$ through configuration interaction, which makes it a likely candidate for the antenna mechanism.

As we see in Fig. 5, the degree of coherence is strongly altered by the removal of $5p_{3/2}^{-1}$ 6*s*, confirming the importance of the Rydberg states in the formation of the antenna. The exact influence of individual states on the antenna efficiency and the final coherence is a topic for future investigations.

4. Antenna transition strength

We now investigate whether there is a correlation between the transitions in the Rydberg manifold that constitute our antenna and the observed variation of the degree of coherence $\tilde{\rho}_{3/2;1/2}$ with the photon energy. The weight of the antenna transition between states *a* and *b* is estimated as

$$w_{ab} = |z_{ab}|^2\big[\min\left(\left|c_{3/2}^{(a)}\right|^2, \left|c_{1/2}^{(a)}\right|^2\right) + \min\left(\left|c_{3/2}^{(b)}\right|^2, \left|c_{1/2}^{(b)}\right|^2\right)\big], \tag{B2}$$

where $c_J^{(s)}$ is the complex amplitude of state *s* in channel *J*. Diagonalizing the field-free Hamiltonian [(A1) with $\hat{V}_L = 0$], we obtain the first 150 excited states and compute (B2) for all dipole-allowed transitions. Those that fall within the energy interval we consider are shown as a stick spectrum in Fig. 6, alongside the degree of coherence. By convoluting the stick spectrum with a Lorentzian

$$\Lambda(\omega) = \frac{1}{1+x^2}, \quad x = \frac{2\omega}{\Gamma}, \tag{B3}$$

where Γ is the FWHM, a continuous distribution is acquired; we use $\Gamma = 5 \times 10^{-4}$ Ha and $h/\Gamma \sim 48$ fs. The similarity of the convoluted spectrum to the degree of coherence is very suggestive, apart from the very strong peak at $\sim$1.56 eV, which is due to a very strong dipole moment for that transition. Exact agreement cannot, however, be expected for a variety of reasons. Equation (B2) considers dipole transitions between field-free states, i.e., disregarding any Stark shifts in the strong field, which means the transitions might not occur at the positions indicated. More important, however, is the fact that we completely disregard the relative populations of the constituent states, which, when prepared through frustrated tunneling, depend strongly on the laser parameters [27].

5. Antenna size

We now wish to estimate the effective size of the antenna structure and relate that to the driving wavelength. In classical electromagnetic theory, a dipole antenna will exhibit the largest gain if the length is $5\lambda/4$; $\lambda/2$ is also very common. Naturally, electron excursions on that scale would far exceed the applicability of the dipole approximation; however, this gives a clear motivation for why large electronic structures are desirable to efficiently couple the external electric field into the atom.

An excited state can, in the CIS ansatz, be written as

$$\sum_k \tilde{\Phi}_k,$$

with the particle orbital $|\tilde{k}\rangle$ containing all information about the electron in the channel associated with excitation or

ionization from the occupied orbital $|k\rangle$. We estimate the size of the state as

$$s_1 \stackrel{\text{def}}{=} \sqrt{\sum_k \langle\tilde{k}|r^2|\tilde{k}\rangle}, \quad s_2 \stackrel{\text{def}}{=} \sum_k \sqrt{\langle\tilde{k}|r^2|\tilde{k}\rangle}.$$

The size of the antenna is then estimated as the geometric mean of the sizes of the two states:

$$\sqrt{s(a)s(b)}.$$

For the transitions in Fig. 6, the estimates fall in the range of 1 to 3 nm, and with a driving wavelength of $\lambda \sim 900$ nm, this corresponds to $\frac{\lambda}{900} - \frac{\lambda}{300}$ antenna structures. This is, of course, far from the optimum $\frac{5\lambda}{4}$ but a lot better than what could be expected from the orbitals of the ground state; $5\{s, p\}$ have a size of ∼0.1 nm, which would yield a $\frac{\lambda}{9000}$ antenna.

6. Coherence due to single Rydberg states

Through resonant excitation, it is possible to generate high degrees of coherence since some Rydberg states have large mixing fractions in $5p_{3/2}^{-1}$ and $5p_{1/2}^{-1}$. If an excited state has equal amplitudes in the two channels, tracing out the excited electron would yield an ionic superposition with a 100% degree of coherence. By choosing the excited state judiciously, we can thus achieve any desired degree of coherence from 0% to 100%. In Fig. 7, we show the mixing coefficients of the first 500 excited states of xenon. Below the $5p_{3/2}^{-1}$ threshold, the $J = 3/2$ component is dominant, with only a few states achieving large fractions of $J = 1/2$. Between the thresholds, the $J = 1/2$ component becomes more important. It is precisely the latter states that Dill [31] considered, studying the importance of the spin-orbit interaction in photoionization.

Can resonant excitation of an intermediate state with high mixing between $5p_{3/2}^{-1}$ and $5p_{1/2}^{-1}$ explain our observed degree of coherence in Fig. 3? Let us first consider weak-field ionization, where through one-photon absorption we populate the intermediate state with energy E_n, which we may write as

$$|\Psi_n\rangle = \mathcal{A}(c_I|I\rangle|n_I\rangle + c_J|J\rangle|n_J\rangle), \tag{B4}$$

where $\mathcal{A}$ is the antisymmetrization operator. Subsequent single-photon ionization will lead to a final state in the form of (2). However, even if c_I and c_J in (B4) are both significant, $w = \langle\chi_I|\chi_J\rangle$ in (2) will still vanish due to energy conservation; the photoelectron peaks will appear at $W_k = \omega - (I_{\mathrm{p},I} - E_n)$ and $W_k = \omega - (I_{\mathrm{p},J} - E_n)$, respectively. This is not the case in the process considered by Dill [31] since the final state involves only one ion channel, namely, $5p_{3/2}^{-1}$, which is populated through direct ionization, as well as autoionization of the intermediately excited states below the $5p_{1/2}^{-1}$ threshold. Thus, energy conservation is automatically fulfilled.

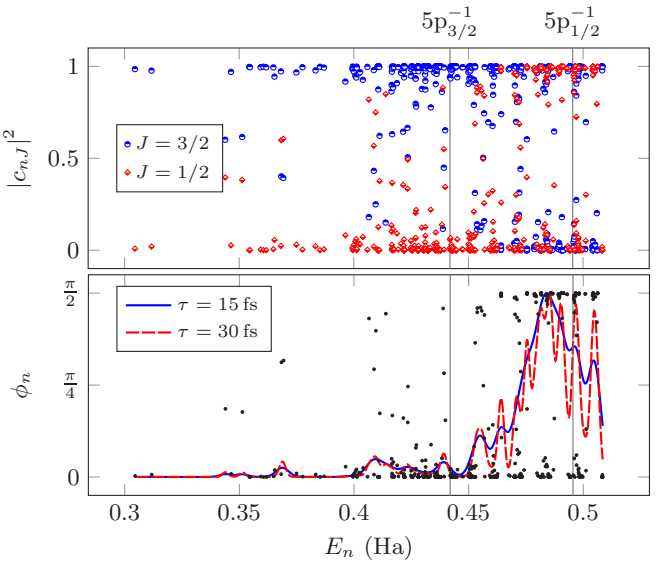

FIG. 7. Rydberg-state channel decomposition for the 500 first excited states of xenon; the top panel shows the populations of state n in $5p_{3/2}^{-1}$ (blue circles) and $5p_{1/2}^{-1}$ (red diamonds) as a function of its excitation energy E_n. The $5s_{1/2}^{-1}$ contributions are negligible for these states. The vertical lines indicate the positions of the ionization thresholds. The bottom panel shows the mixing angle $\phi_n \stackrel{\text{def}}{=} \arctan(|c_{n;1/2}|/|c_{n;3/2}|)$; $\phi_n = 0$ indicates a state purely in $5p_{3/2}^{-1}$, $\phi_n = \pi/2$ indicates a state purely in $5p_{1/2}^{-1}$, and $\phi_n = \pi/4$ indicates an even mixture. The lines show the average mixing angle as a function of excitation energy when convolving with a Gaussian corresponding to 15-fs duration (solid blue line) and 30-fs duration (dashed red line).

We next consider strong-field ionization. In this case, it is difficult to address a single state. Instead, we access the average coherence of the state manifold, which remains low; see the average mixing angle in the bottom panel of Fig. 7. Furthermore, subsequent ionization and generation of ATI progressions would still face the same predicament as stated earlier: for $\eta \sim 1$, photoelectron peaks with similar kinetic energy would result from absorption of different numbers of photons, and thus by parity, their overlap would vanish. The atomic antenna, which repeatedly accesses parts of the excited spectrum with high mixing fractions, allows us to amplify this small, average mixing coefficient.

[1] J. Wragg, D. D. A. Clarke, G. S. J. Armstrong, A. C. Brown, C. P. Ballance, and H. W. van der Hart, Resolving Ultrafast Spin-orbit Dynamics in Heavy Many-Electron Atoms, Phys. Rev. Lett. **123**, 163001 (2019).

[2] M. Kübel, Z. Dube, A. Y. Naumov, D. M. Villeneuve, P. B. Corkum, and A. Staudte, Spatiotemporal imaging of valence electron motion, Nat. Commun. **10**, 1042 (2019).

[3] E. Goulielmakis, Z.-H. Loh, A. Wirth, R. Santra, N. Rohringer, V. S. Yakovlev, S. Zherebtsov, T. Pfeifer, A. M. Azzeer, M. F. Kling, S. R. Leone, and F. Krausz, Real-time observation of valence electron motion, Nature (London) **466**, 739 (2010).

[4] A. Hartung, F. Morales, M. Kunitski, K. Henrichs, A. Laucke, M. Richter, T. Jahnke, A. Kalinin, M. Schöffler, L. P. H. Schmidt, M. Ivanov, O. Smirnova, and R. Dörner, Electron spin polarization in strong-field ionization of xenon atoms, Nat. Photonics **10**, 526 (2016).

[5] I. Barth and O. Smirnova, Spin-polarized electrons produced by strong-field ionization, Phys. Rev. A **88**, 013401 (2013).

[6] I. Barth and O. Smirnova, Hole dynamics and spin currents after ionization in strong circularly polarized laser fields, J. Phys. B **47**, 204020 (2014).

[7] M. Yu. Kuchiev, Atomic antenna, Pis. Zh. Eksp. Teor. Fiz. **45**, 319 (1987) [JETP Lett. **45**, 404 (1987)].

[8] M. E. Tzur, O. Neufeld, A. Fleischer, and O. Cohen, Selection rules for breaking selection rules, New J. Phys. **23**, 103039 (2021).

[9] R. K. Nesbet, Configuration interaction in orbital theories, Proc. R. Soc. London, Ser. A **230**, 312 (1955).

[10] P.-O. Löwdin, Quantum theory of many-particle systems. I. Physical interpretations by means of density matrices, natural spin-orbitals, and convergence problems in the method of configurational interaction, Phys. Rev. **97**, 1474 (1955).

[11] P. Krause, T. Klamroth, and P. Saalfrank, Time-dependent configuration-interaction calculations of laser-pulse-driven many-electron dynamics: Controlled dipole switching in lithium cyanide, J. Chem. Phys. **123**, 074105 (2005).

[12] N. Rohringer, A. Gordon, and R. Santra, Configuration-interaction-based time-dependent orbital approach for *ab initio* treatment of electronic dynamics in a strong optical laser field, Phys. Rev. A **74**, 043420 (2006).

[13] L. Greenman, P. J. Ho, S. Pabst, E. Kamarchik, D. A. Mazziotti, and R. Santra, Implementation of the time-dependent configuration-interaction singles method for atomic strong-field processes, Phys. Rev. A **82**, 023406 (2010).

[14] S. Carlström, M. Spanner, and S. Patchkovskii, General time-dependent configuration-interaction singles. I. Molecular case, Phys. Rev. A **106**, 043104 (2022); S. Carlström, M. Bertolino, J. M. Dahlström, and S. Patchkovskii, General time-dependent configuration-interaction singles. II. Atomic case, **106**, 042806 (2022).

[15] K. A. Peterson, D. Figgen, E. Goll, H. Stoll, and M. Dolg, Systematically convergent basis sets with relativistic pseudopotentials. II. Small-core pseudopotentials and correlation consistent basis sets for the post-d group 16–18 elements, J. Chem. Phys. **119**, 11113 (2003).

[16] F. Zapata, J. Vinbladh, A. Ljungdahl, E. Lindroth, and J. M. Dahlström, Relativistic time-dependent configuration-interaction singles method, Phys. Rev. A **105**, 012802 (2022).

[17] A. M. Ermolaev, I. V. Puzynin, A. V. Selin, and S. I. Vinitsky, Integral boundary conditions for the time-dependent Schrödinger equation: Atom in a laser field, Phys. Rev. A **60**, 4831 (1999).

[18] A. M. Ermolaev and A. V. Selin, Integral boundary conditions for the time-dependent Schrödinger equation: Superposition of the laser field and a long-range atomic potential, Phys. Rev. A **62**, 015401 (2000).

[19] V. V. Serov, V. L. Derbov, B. B. Joulakian, and S. I. Vinitsky, Wave-packet evolution approach to ionization of the hydrogen molecular ion by fast electrons, Phys. Rev. A **63**, 062711 (2001).

[20] L. Tao and A. Scrinzi, Photo-electron momentum spectra from minimal volumes: The time-dependent surface flux method, New J. Phys. **14**, 013021 (2012).

[21] A. Scrinzi, t-SURFF: Fully differential two-electron photoemission spectra, New J. Phys. **14**, 085008 (2012).

[22] F. Morales, T. Bredtmann, and S. Patchkovskii, iSURF: A family of infinite-time surface flux methods, J. Phys. B **49**, 245001 (2016).

[23] S. Pabst, M. Lein, and H. J. Wörner, Preparing attosecond coherences by strong-field ionization, Phys. Rev. A **93**, 023412 (2016).

[24] M. Ruberti, P. Decleva, and V. Averbukh, Full *ab initio* many-electron simulation of attosecond molecular pump-probe spectroscopy, J. Chem. Theory Comput. **14**, 4991 (2018).

[25] M. Ruberti, Onset of ionic coherence and ultrafast charge dynamics in attosecond molecular ionisation, Phys. Chem. Chem. Phys. **21**, 17584 (2019).

[26] M. Ruberti, Quantum electronic coherences by attosecond transient absorption spectroscopy: *Ab initio* B-spline RCS-ADC study, Faraday Discuss. **228**, 286 (2021).

[27] T. Nubbemeyer, K. Gorling, A. Saenz, U. Eichmann, and W. Sandner, Strong-Field Tunneling without Ionization, Phys. Rev. Lett. **101**, 233001 (2008).

[28] U. Eichmann, T. Nubbemeyer, H. Rottke, and W. Sandner, Acceleration of neutral atoms in strong short-pulse laser fields, Nature (London) **461**, 1261 (2009).

[29] H. Zimmermann, S. Patchkovskii, M. Ivanov, and U. Eichmann, Unified Time and Frequency Picture of Ultrafast Atomic Excitation in Strong Laser Fields, Phys. Rev. Lett. **118**, 013003 (2017).

[30] R. R. Freeman, P. H. Bucksbaum, H. Milchberg, S. Darack, D. Schumacher, and M. E. Geusic, Above-Threshold Ionization with Subpicosecond Laser Pulses, Phys. Rev. Lett. **59**, 1092 (1987).

[31] D. Dill, Resonances in photoelectron angular distributions, Phys. Rev. A **7**, 1976 (1973).

[32] J. A. R. Samson and J. L. Gardner, Resonances in the Angular Distribution of Xenon Photoelectrons, Phys. Rev. Lett. **31**, 1327 (1973).

[33] E. B. Saloman, Energy levels and observed spectral lines of xenon, Xe I through Xe LIV, J. Phys. Chem. Ref. Data **33**, 765 (2004).

[34] G. Petite, P. Agostini, and F. Yergeau, Intensity, pulse width, and polarization dependence of above-threshold-ionization electron spectra, J. Opt. Soc. Am. B **4**, 765 (1987).

[35] S. Carlström, J. Mauritsson, K. J. Schafer, A. L'Huillier, and M. Gisselbrecht, Quantum coherence in photo-ionisation with tailored XUV pulses, J. Phys. B **51**, 015201 (2018).

[36] D. A. Varshalovich, *Quantum Theory of Angular Momentum: Irreducible Tensors, Spherical Harmonics, Vector Coupling Coefficients, 3nj Symbols* (World Scientific, Singapore, 1988).

[37] S. L. Adler and T. Piran, Relaxation methods for gauge field equilibrium equations, Rev. Mod. Phys. **56**, 1 (1984).

[38] J. L. Krause and K. J. Schafer, Control of THz emission from Stark wave packets, J. Phys. Chem. A **103**, 10118 (1999).

[39] R. Garstang, Transition probabilities of forbidden lines, J. Res. Natl. Bur. Stand., Sect. A **68A**, 61 (1964).

[40] D. K. Nandy and B. K. Sahoo, Forbidden transition properties in the ground-state configurations of singly ionized noble gas atoms for stellar and interstellar media, Mon. Not. R. Astron. Soc. **450**, 1012 (2015).

[41] M. Dolg and X. Cao, Relativistic pseudopotentials: Their development and scope of applications, Chem. Rev. **112**, 403 (2012).

[42] D. E. Manolopoulos, Derivation and reflection properties of a transmission-free absorbing potential, J. Chem. Phys. **117**, 9552 (2002).

[43] S. Patchkovskii and H. Muller, Simple, accurate, and efficient implementation of 1-electron atomic time-dependent Schrödinger equation in spherical coordinates, Comput. Phys. Commun. **199**, 153 (2016).

[44] W. Fritsch and C.-D. Lin, The semiclassical close-coupling description of atomic collisions: Recent developments and results, Phys. Rep. **202**, 1 (1991).

[45] R. Jankowiak, J. M. Hayes, and G. J. Small, Spectral hole-burning spectroscopy in amorphous molecular solids and proteins, Chem. Rev. **93**, 1471 (1993).

[46] E. Goll, G. Wunner, and A. Saenz, Formation of Ground-State Vibrational Wave Packets in Intense Ultrashort Laser Pulses, Phys. Rev. Lett. **97**, 103003 (2006).